Journal of Power Sources 239 (2013) 157–163

Contents lists available at SciVerse ScienceDirect

Journal of Power Sources

journal homepage: www.elsevier.com/locate/jpowsour

Self-assembled porous $NiCo_2O_4$ hetero-structure array for electrochemical capacitor

X.Y. Liu, Y.Q. Zhang, X.H. Xia, S.J. Shi, Y. Lu, X.L. Wang, C.D. Gu, J.P. Tu*

State Key Laboratory of Silicon Materials, Key Laboratory of Advanced Materials and Applications for Batteries of Zhejiang Province and Department of Materials Science and Engineering, Zhejiang University, Hangzhou 310027, China

HIGHLIGHTS

- Porous $NiCo_2O_4$ hetero-structure arrays on nickel foam were prepared by facile hydrothermal method.
- The porous $NiCo_2O_4$ hetero-structure array exhibits excellent pseudocapacitive properties.
- The specific capacitance achieves a maximum of 1089 F g^{-1} at a current density of 2 A g^{-1}.
- The specific capacitance can still retain 1058 F g^{-1} (97.2% retention) after 8000 cycles.

ARTICLE INFO

Article history:
Received 19 December 2012
Received in revised form
6 March 2013
Accepted 21 March 2013
Available online 30 March 2013

Keywords:
Spinel nickel cobaltate
Porous film
Hetero-structure
Supercapacitor

ABSTRACT

Porous $NiCo_2O_4$ hetero-structure arrays on nickel foam are prepared by a facile hydrothermal method. The morphology of the arrays changes with the growth time. After hydrothermal synthesis for 8 h in combination with annealing treatment, the $NiCo_2O_4$ array presents a nanoflake–nanowire hetero-structure. The porous $NiCo_2O_4$ hetero-structure array exhibits the excellent pseudocapacitive properties in 2 M KOH, with a high capacitance of 891 F g^{-1} at 1 A g^{-1} and 619 F g^{-1} at 40 A g^{-1} before activation as well as excellent cycling stability. The specific capacitance can achieve a maximum of 1089 F g^{-1} at a current density of 2 A g^{-1}, which can still retain 1058 F g^{-1} (97.2% retention) after 8000 cycles. The enhanced pseudocapacitive performances are mainly attributed to its unique hetero-structure which provides fast ion and electron transfer, large reaction surface area and good strain accommodation.

1. Introduction

Of the various advanced energy storage and power sources, supercapacitors represent an emerging technology that offers fast recharge ability, high power density and long cycle life [1–7]. Early studies of supercapacitors mainly focus on carbonaceous materials, which suffer from relatively low specific capacitance and instability at a high charge–discharge rate. In recent years, supercapacitors based on pseudocapacitive materials have evoked considerable interest [8–10]. Among them, RuO_2 is noteworthy for its specific capacity as high as 1580 F g^{-1}. However, the commercialization is not promising for its high cost and rareness. Therefore, great efforts have been devoted to searching for inexpensive alternative transition metal oxides with good capacitive characteristics [2,11–13], especially those who possess multiple oxidation states/structures that enable rich redox reactions, such as Co_3O_4 [14,15], NiO [10,16,17], MnO_2 [18–20] and hydroxide-based composites [21–25], Co_3O_4/NiO core/shell nanowire arrays [26]. Recently, binary metal oxide systems have evoked tremendous interest for the combined contributions from both the metal ions [27–31]. $NiCo_2O_4$ is such an attractive pseudocapacitive material since it offers many intriguing advantages of good environmental compatibility and high specific capacitance.

$NiCo_2O_4$ is generally regarded as a mixed valence oxide that adopts a pure spinel structure. It has been reported to possess a much better electronic conductivity and higher electrochemical activity than those of the two corresponding single component oxides [2,9,32–43]. So far, $NiCo_2O_4$ materials have drawn intensive research attention in supercapacitors. Earlier, Wei et al. [2] reported a novel epoxide-driven sol–gel process to prepare $NiCo_2O_4$ aerogels, with an ultrahigh specific capacity. Despite high capacitance, pseudocapacitive materials often present a compromise between the power performance and reversibility due to the slow kinetics of ion and electron transport in electrodes and at the electrode/

* Corresponding author. Tel.: +86 571 87952856; fax: +86 571 87952573.
E-mail addresses: tujp@zju.edu.cn, tujplab@zju.edu.cn (J.P. Tu).

0378-7753/$ – see front matter © 2013 Elsevier B.V. All rights reserved.
http://dx.doi.org/10.1016/j.jpowsour.2013.03.106

electrolyte interface. To our knowledge, a golden way to enhance the redox kinetics is to create porous nanostructures with large surface area and short diffusion path of ions and electrons. To date, $NiCo_2O_4$ structures such as nanowires, nanosheets and urchin-like nanostructures have been synthesized by using hydrothermal process [36,38,44], polyethylene glycol-directed technique [45], and potentiostatic deposition [13]. However, most of these materials often suffer from low capacitance and/or poor cycling stability. Typically, Jiang et al. [45] reported hierarchical porous $NiCo_2O_4$ nanowires for supercapacitor application. Despite its excellent rate capability, the specific capacity and cycling stability are far from satisfactory. Besides, Wang et al. [38] and Wu et al. [44] reported urchin-like $NiCo_2O_4$ nanostructures by hydrothermal method free of template and catalyst, the cycling stability can not meet industrial application as well. Based on the above considerations, one would expect $NiCo_2O_4$ arrays with new structures to be a promising candidate for the construction of high performance supercapacitors.

In this present work, a new self-assembled porous hetero-structure $NiCo_2O_4$ array on nickel foam is synthesized via a hydrothermal method coupled with a post annealing treatment. After the hydrothermal reaction for 8 h, we successfully obtained $NiCo_2O_4$ array with a unique nanoflake–nanowire hetero-structure. Impressively, the porous $NiCo_2O_4$ hetero-structure array exhibits noticeable pseudocapacitive performance with high capacitance as well as excellent cycling stability. Due to the unique properties of these nanoflake–nanowire arrays, such as high surface areas, good conductivity and direct growth on conductive substrates, they have potential applications in energy conversion storage.

2. Experimental

All the reagents used in the experiment were of analytical grade. The cobalt nitrate, nickel nitrate, urea and ammonium fluoride were obtained from Shanghai Chemical Reagent Co. All aqueous solutions were freshly prepared with high purity water (18 MΩ cm resistance).

Self-assembled porous $NiCo_2O_4$ arrays were synthesized on nickel foam by a facile hydrothermal method. The experimental details were as follows. 1 mmol of $Ni(NO_3)_2$, 2 mmol of $Co(NO_3)_2$, 6 mmol of NH_4F and 15 mmol of urea were dissolved in 70 mL of deionized water under magnetical stirring for 30 min in air. Nickel foam substrate with 3.5 × 5.0 cm in size was pressed to a thin plate under a pressure of 10 MPa and cleaned ultrasonically in ethanol for 15 min. Its top side was protected from solution contamination by uniformly coating with a polytetrafluoroethylene tape. Then the resulting solution was transferred into a 100 mL Teflon-lined stainless steel autoclave and the nickel foam substrate was immersed into it. After that, the autoclave was heated to 120 °C inside a conventional oven for different times, and then allowed to cool to room temperature naturally. Subsequently, the pink precursor was removed from the solution and washed with distilled water repeatedly. Since the precursor is cobalt–nickel hydroxide, it converts into cobalt–nickel oxide after annealing at 350 °C for 2 h in flowing argon.

The loading mass of $NiCo_2O_4$ which was hydrothermal synthesized for 8 h was 1.8 mg cm^{-2}. The weight of the $NiCo_2O_4$ grown on Ni foam was measured by calculating the mass between Ni foam and the $NiCo_2O_4$ product after the hydrothermal reaction and heat treatment. Finally, the specific mass was obtained by dividing the total mass of $NiCo_2O_4$ by the area.

Thermogravimetric and differential thermal analysis (TG-DTA) of the hydroxide precursor were measured on a Pyris 1 TGA apparatus in the temperature range of 40–600 °C at a heating rate of 7 °C min^{-1}. The structures and morphologies of the products were characterized by X-ray diffraction (XRD, RIGAKU D/Max-2550 with Cu Kα radiation), field emission scanning electron microscopy (FESEM, FEI SIRION) and transmission electron microscopy (TEM, JEOL JEM200CX, JEM-2010F). The chemical composition of the products was determined by means of energy dispersive X-ray spectroscopy (EDX attached to TEM, JEOL JEM200CX). The specific surface areas were measured following the multipoint Brunauer–Emmett–Teller (BET) procedure from the N_2 adsorption–desorption isotherms using an AUTOSORB-1-C gas sorption analyzer.

A three-electrode cell was used for electrochemical measurements with a nickel mesh and Hg/HgO as the counter and reference electrodes, respectively. 2.0 M KOH aqueous solution was used as the electrolyte and all the electrochemical measurements were conducted at room temperature. Cyclic voltammetry (CV) measurements were performed on a CHI660D electrochemical workstation (Chenhua, Shanghai) at a scan rate of 10 mV s^{-1} between 0 and 0.55 V. The galvanostatic charge–discharge tests were conducted on a LAND battery program-control test system. The specific capacitance is calculated according to the following equation:

$$C = \frac{I\Delta t}{M\Delta V} \quad (1)$$

where C (F g^{-1}) is the specific capacitance, I (mA) represents the discharge current, and M (mg), ΔV (V) and Δt (s) designates the mass of active materials, potential drop during discharge and total discharge time, respectively. Energy density (E) is derived from the following equation:

$$E = \frac{1}{2}C\Delta V^2 \quad (2)$$

Power density (P) is calculated from the following equation:

$$P = \frac{E}{\Delta t} \quad (3)$$

3. Results and discussion

3.1. Synthesis and characterization

Fig. 1 shows the XRD patterns of the precursor and the final $NiCo_2O_4$ films hydrothermal synthesized for 8 h. Besides three strong peaks from the nickel foam substrate, all the reflection peaks of the precursor film can be well indexed to nickel cobalt hydroxide $Ni_{0.988}Co_{0.012}(OH)_2$ (JCPDS 59-0461) (Fig. 1a). After heat treatment, all the diffraction peaks are attributed to spinel $NiCo_2O_4$ phase

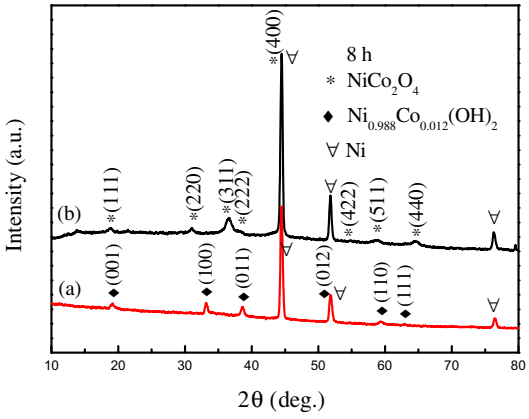

Fig. 1. XRD patterns of the precursor (a) and the final $NiCo_2O_4$ nanoflake–nanowire arrays (b) after hydrothermal synthesis for 8 h.

(JCPDS 73-1702), indicating that the $NiCo_2O_4$ crystalline has been formed after annealing treatment (Fig. 1b).

A thermogravimetric and differential thermal analysis (TG-DTA) curve of the Ni–Co hydroxide precursor hydrothermal synthesized for 8 h in air is shown in Fig. 2. It can be seen that the Ni–Co hydroxide begins to decompose at 280 °C. In the DTA curve, there is a strong heat absorption peak at around 339 °C, which is caused by decomposition of Ni–Co hydroxide to $NiCo_2O_4$. The result shows that it is reasonable to set the annealing temperature at 350 °C.

SEM images of the final product and precursor hydrothermal synthesized for 8 h are presented in Fig. 3. Apparently, the morphology of the product before and after annealing does not change much, maintaining the hetero-architecture. The growth process for the nanoflake–nanowire $NiCo_2O_4$ array can be interpreted by inspecting the morphologies at different growth stages by controlling the time. After reacting for 3 h, the skeletons of nickel foam are uniformly decorated with thin nanoflakes and no nanowire appears (Fig. 3a). With increasing the reaction time, the nanowires grow at the edge of the nanoflakes with a cross configuration at the base (Fig. 3b–e), finally producing the interesting heterostructured array. After reacting for 8 h, nanowires stand at the edge of the nanoflakes. The $NiCo_2O_4$ nanowires have an average diameter of 100 nm and length up to around 2 μm (Fig. 3f). Clearly, no nanowires packed in the interspaces of the nanoflakes, indicating that nanowires were preferentially deposited at the edge. Meanwhile, the length of nanowires could be easily controlled by the growth time.

The structural characteristics of the product hydrothermal synthesized for 8 h combined with annealing treatment are further investigated, as shown in Fig. 4. The $NiCo_2O_4$ hetero-structure arrays were scratched down from the Ni foam, and the structural characteristics of the nanoflakes and nanowires were analyzed. Typical TEM image reveals that nanoflakes and nanowires coexist in the array, further confirming the hetero-architecture. The $NiCo_2O_4$ nanowire and nanoflake can be easily distinguished. Both the nanowire (Fig. 4a) and nanoflake (Fig. 4b) consist of numerous interconnected nanoparticles and present a mesoporous structure, which is ascribed to the successive release and lose of CO_2 and H_2O during the thermal decomposition of precursor. The selected-area electron diffraction (SAED) patterns of both the nanowire and nanoflake are presented in Fig. 4c and d, respectively. Apparently, SAED patterns are almost identical between the nanowire and nanoflake. They can be well indexed to the spinel structure. Furthermore, both of them show well-defined rings, indicating their polycrystalline characteristics. Fig. 4e and f shows the HRTEM images recorded from the nanowire and nanoflake. The lattice fringes with a lattice spacing of about 0.467 and 0.461 nm corresponds to the (111) plane of $NiCo_2O_4$, indicating that the nanowire and nanoflake share a same nanostructure.

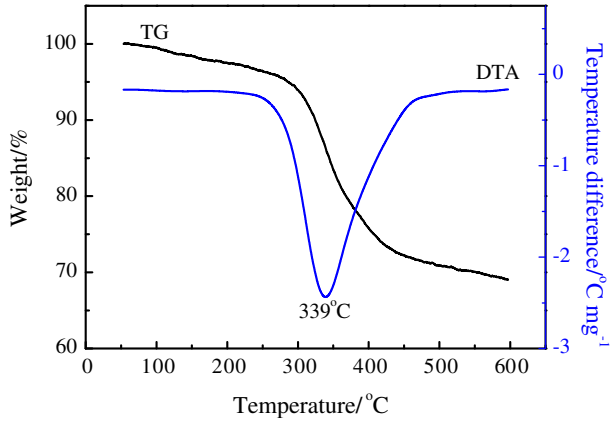

Fig. 2. TG and DTA curves for the precursor after hydrothermal synthesis for 8 h.

The relative proportions of element Ni and Co in the nanowire and nanoflake of the $NiCo_2O_4$ nanoflake–nanowire array hydrothermal synthesized for 8 h have been investigated using EDX analysis (Fig. S1). The results show the presence of Co and Ni both in nanowires and nanoflakes, with an average atomic ratio of Co:Ni of ~1.4 in the nanoflake, while an average atomic ratio of Co:Ni is ~1.8 in the nanowire, which is close to the stoichiometric molar ratio of 2:1 in the nanowire. The nanoflake is relatively enriched in Ni, where much of the Co atom positions in the spinel structure are substituted by Ni. In the periodic table, Co (No. 27) is next to Ni (No. 28), and the radii of Co and Ni atom are close. As a result, the change in atom placement (Co replaced by Ni) has brought about a very small change in the Ni–Co spinel structure, and this has not been reflected in the corresponding SAED analysis [46].

Here, a general growth mechanism for the unique hetero-structure is suggested, based on above analysis, as shown schematically in Fig. 5. Most likely, it is due to the difference between the solubility product (K_{sp}) of nickel-rich (nanoflake) and nickel-poor (nanowire) products. K_{sp} reflects the dissolving ability of the insoluble electrolyte in solution. As the reaction proceeds, mesocrystals with a common crystallographic orientation begin to appear in the supersaturated solution. Then they join together to form particles at a planar interface. It is easier for the nickel-rich particles to deposit because K_{sp} of the nickel-rich product is lower than that of the nickel-poor (cobalt-rich) one. As a result, the nickel-rich particles play a dominant role in the beginning of the growth process, which leads to the formation of nanoflakes. Meanwhile, the EDX results also validate the hypothesis for a relatively high Ni content in the nanoflake. Considering that the original ratio of the Co^{2+}/Ni^{2+} is 2:1 in the solution, while Co^{2+} and Ni^{2+} react in a ratio lower than 2:1 to form the $NiCo_2O_4$ spinel phase precipitation, there would leave some surplus Co^{2+} in the solution as the process proceeds. Such surplus Co^{2+} atom is the reason for the growth of nanowires (nickel-poor product). The stoichiometric cobalt–nickel hydroxide particles (nickel-poor particles) begin to grow after the supersaturated solution with such particles is formed, forming active nucleation centers by reducing the surface energy. At this time, the nanoflakes act as the backbone to guide the deposition of such particles. The cobalt-rich particles prefer to deposit at the edge of nanoflakes because the surface energy here is higher than that at the plain surface. Finally, the self-assembled porous $NiCo_2O_4$ hetero-structure array is produced after annealing.

The BET surface area of the final $NiCo_2O_4$ products hydrothermal synthesized for 3, 5, 7, 8, 12 h are 57.26, 73.20, 82.08, 99.96, 78.54, respectively (see Supporting information, Fig. S2). It is clearly seen that the one synthesized for 8 h gives the highest BET value. Although the product grown for 12 h also presents a hetero-architecture, the interspace between the arrays is much smaller than that of the product grown for 8 h, which results in harder electrolyte penetration into the inner region of the electrode. In short, the one grown for 8 h is expected to exhibit better electrochemical properties than the other products. The pore size distribution of the $NiCo_2O_4$ synthesized for 8 h is presented in the inset of Fig. S2d. It can be seen that the product contains a distribution of macropores in the range of 30–120 nm. Such a porous structure permits easy access for the redox reactions.

3.2. Electrochemical analysis

To evaluate the capacitive performance of the porous hetero-structured array grown for 8 h, CV and galvanostatic charge–

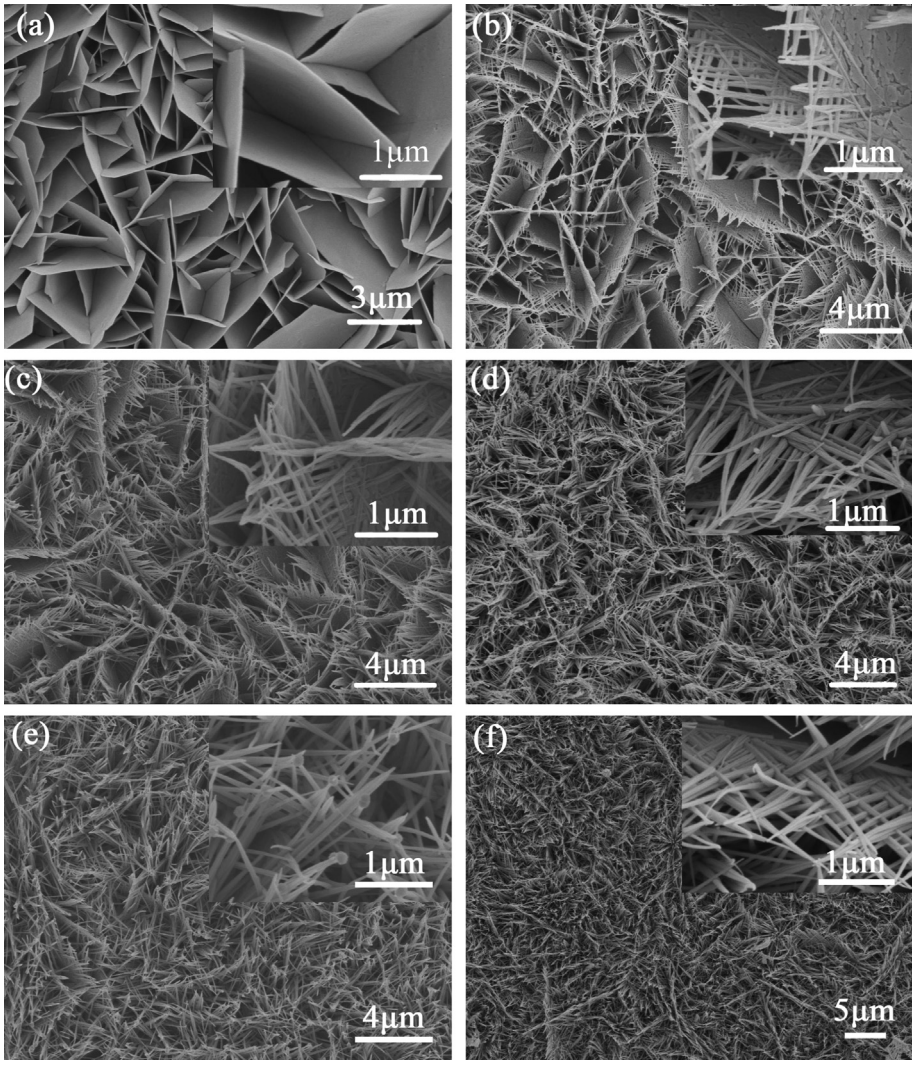

Fig. 3. SEM images of the final products after hydrothermal synthesis for different times: (a) 3 h; (b) 5 h; (c) 7 h; (d) 8 h; (e) 12 h; (f) the precursor obtained after hydrothermal reaction for 8 h.

discharge measurements were carried out in 2.0 M KOH aqueous solution. The CV curves of the porous $NiCo_2O_4$ array and nickel foam are presented in Fig. 6a. For the porous $NiCo_2O_4$ hetero-structure array, only one oxidation peak P1 is observed in the anodic process and two reduction peaks P2, P3 are noticed in the cathodic process, which indicates that the capacitive characteristics are mainly governed by Faradic reaction. It is justified that the oxidation peak P1 is an integrated peak of two small ones. The two pairs of redox current peaks correspond to the reversible reactions of Co^{2+}/Co^{3+} and Ni^{2+}/Ni^{3+} transitions. The redox reactions in the alkaline electrolyte are based on the following equations [21]:

$$NiCo_2O_4 + OH^- + H_2O \leftrightarrow NiOOH + 2CoOOH + 2e^- \quad (4)$$

$$CoOOH + OH^- \leftrightarrow CoO_2 + H_2O + e^- \quad (5)$$

It is known that the substrate has a nontrivial influence on the electrochemical performance. To check the substrate effect of Ni foam, we also present the CV curve of nickel foam. It is noted that the nickel foam shows a redox process A1/A2 with low current intensities. This redox couple is attributed to the reversible reaction of Ni(II)/Ni(III) formed on the nickel surface. Compared to the porous heterostructured array, however, the signal of nickel foam is quite small, indicating that the nickel foam contributes little to the total capacitance of the electrode.

Fig. 6b shows the discharge curves of the porous $NiCo_2O_4$ hetero-structure array in a potential range of 0–0.55 V at current densities between 1 and 40 A g^{-1}. Besides, the relationship between the specific capacitance or capacity retention and current density are illustrated in Fig. 6c. The nonlinear charge/discharge curves further verify the pseudo-capacitance behavior. In our experiment, all specific capacitances are calculated by subtracting the discharge time of nickel foam and reducing the substrate effect to the lowest level. Before activation, the porous $NiCo_2O_4$ hetero-structure array exhibits pseudo-capacitances with 891 F g^{-1} at 1 A g^{-1}, 849 F g^{-1} at 2 A g^{-1}, 812 F g^{-1} at 4 A g^{-1}, 757 F g^{-1} at 10 A g^{-1}, 709 F g^{-1} at 20 A g^{-1}, 619 F g^{-1} at 40 A g^{-1}, respectively. 70% of capacitance is retained when the discharge current density changes from 1 A g^{-1} to 40 A g^{-1}. Such high specific capacitance is superior to the other $NiCo_2O_4$-based electrodes in different configurations, such as hierarchical porous $NiCo_2O_4$ nanowires (743 F g^{-1} at 1 A g^{-1} after activation) [45], $NiCo_2O_4$ nanosheets on stainless-steel sheet (575 F g^{-1} at

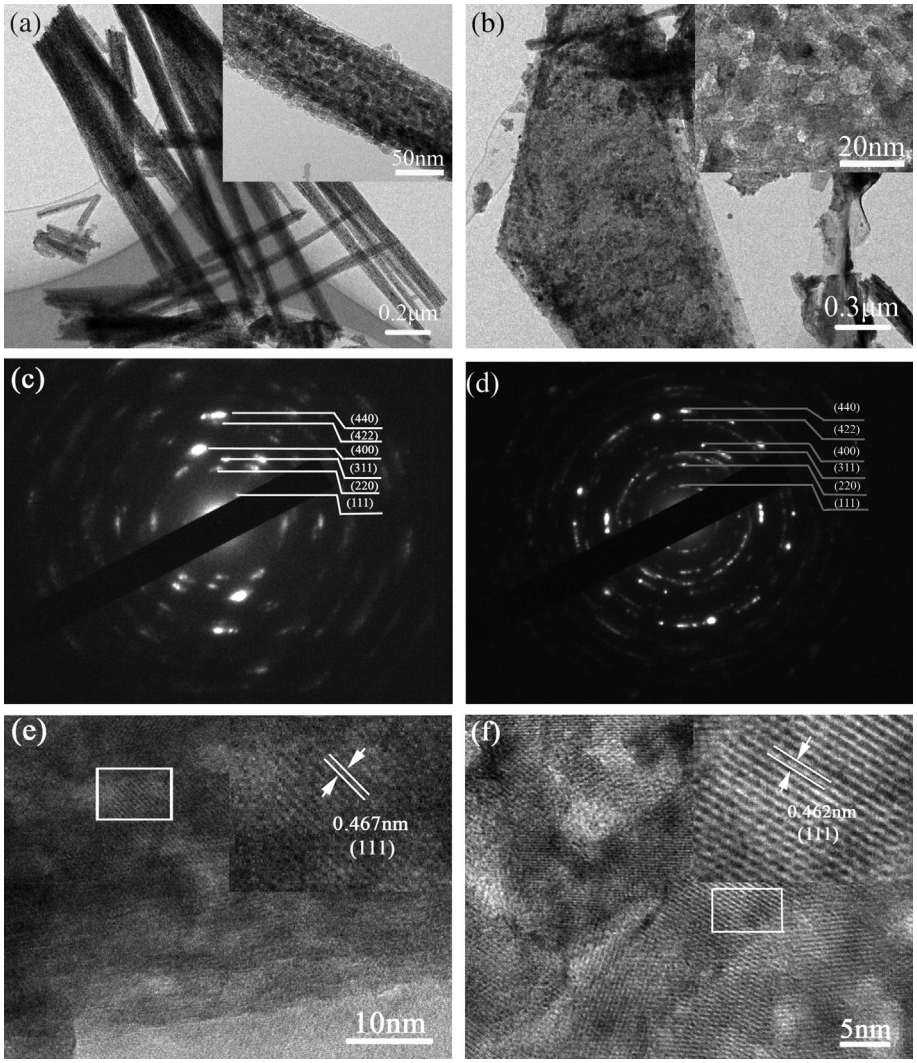

Fig. 4. TEM images of the nanowire (a) and nanoflake (b) in the $NiCo_2O_4$ nanoflake–nanowire array, SAED patterns of the nanowire (c) and nanoflake (d) in the $NiCo_2O_4$ nanoflake–nanowire array, HRTEM images of the nanowire (e) and nanoflake (f) in the $NiCo_2O_4$ nanoflake–nanowire array.

1 A g^{-1}) [13], urchin-like microspherical superstructures which was also prepared by hydrothermal method (296 F g^{-1} at 1 A g^{-1}) [44], and other powder forms [2,33]. Typically, Jiang and co-worker developed a facile polyethylene glycol-directed technique at room temperature to synthesize hierarchical porous $NiCo_2O_4$ nanowires which exhibit a high specific capacitance of 743 F g^{-1} at 1 A g^{-1} [45]. It is the unique properties of the $NiCo_2O_4$ hetero-architecture array that results in the high specific capacitance and fast redox kinetics. The large opened "V-type" channels between nanoflakes and the richer redox reactions from both nickel and cobalt ions contribute to the high specific capacitance.

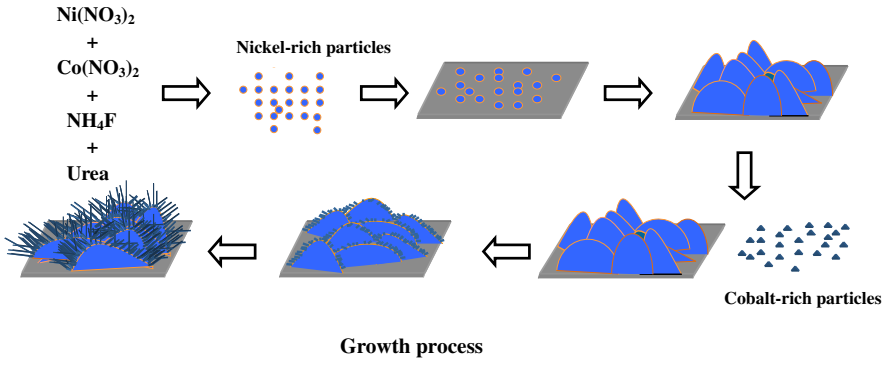

Fig. 5. Schematic illustration of the growth process for self-assembled porous $NiCo_2O_4$ array.

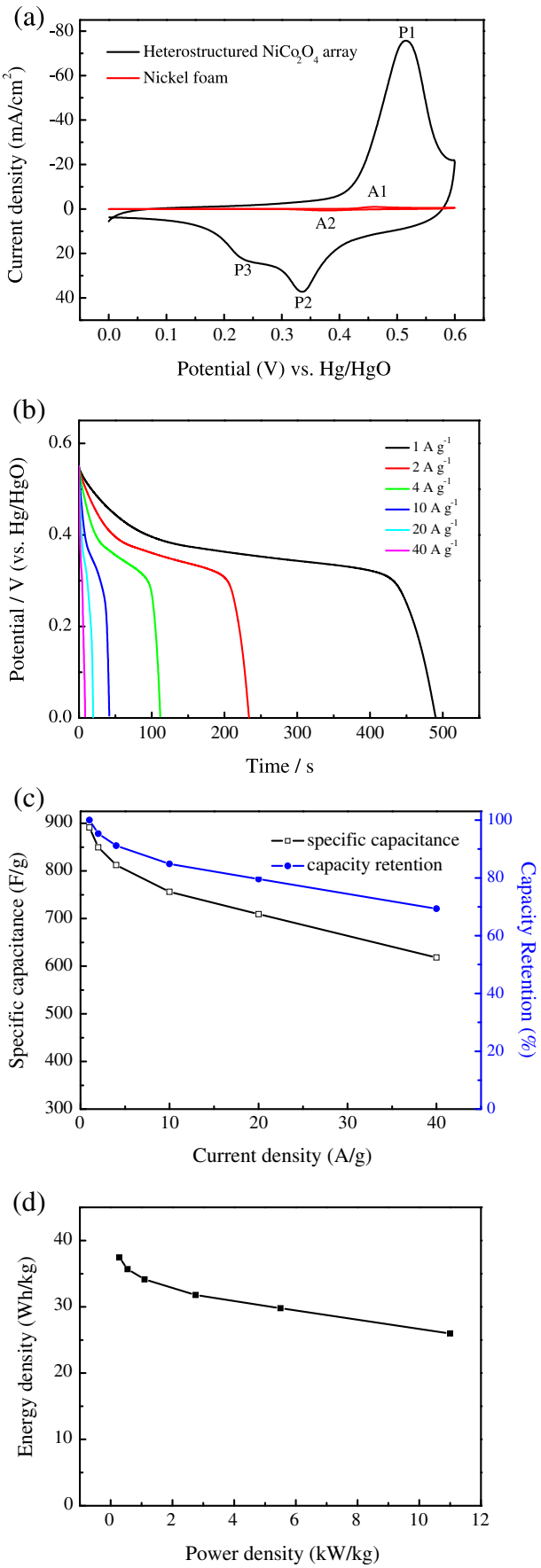

Ragone plot (power density vs. energy density) is also presented in Fig. 6d. The energy density can be estimated to be 37.5 Wh kg^{-1} at a power density of 275 W kg^{-1}, which is also superior to other $NiCo_2O_4$ materials [13,38]. More significantly, the energy density of the $NiCo_2O_4$ electrode is still as high as 26 Wh kg^{-1} at a high power density of 11 kW kg^{-1}. These encouraging results further illustrate that the porous $NiCo_2O_4$ hetero-structure array is a promising electrode material for supercapacitors.

The enhancement in the supercapacitor performance of the porous $NiCo_2O_4$ hetero-structure array can also be manifested by its excellent cycling stability. Fig. 7 shows the cyclability of the porous $NiCo_2O_4$ array over 8000 cycles between 0 and 0.5 V at a current density of 2 A g^{-1}. It can be observed that the specific capacitance increases gradually in the first 3000 cycles, which can be attributed to the complete activation of the electrode. At a cycle number of 3000, the specific capacitance reaches a maximum value of 1089 F g^{-1}. The loss in specific capacitance based on this maximum value is only about 2.8% after 8000 cycles. The cycling performance is much better than that of other $NiCo_2O_4$-based nanostructures, such as hierarchical porous $NiCo_2O_4$ nanowires (~6.2% loss after 3000 cycles) [45], (~6.2% loss after 3000 cycles) [36], single-crystalline $NiCo_2O_4$ nanoneedle arrays (~5.26% loss after 2000 cycles) [39], $NiCo_2O_4$ nanosheets (575 F g^{-1} at 1 A g^{-1}) [13], urchin-like $NiCo_2O_4$ nanostructures which was also prepared by hydrothermal method (~9.2% loss after 2000 cycles) [44] and $NiCo_2O_4$ aerogels (~6% loss after 2000 cycles) [2]. The stable and connecting structure helps to alleviate the structure damage caused by volume expansion during cycling process, resulting in an enhanced stability. Besides, the porous feature is also reckoned to digest the possible volume changes while cycling.

The enhanced pseudo-capacitances and excellent cycling stability of the $NiCo_2O_4$ array can be ascribed to the unique hetero-architecture. First, the large opened "V-type" channels between nanoflakes enable the full exposure of both nanoflake and nanowire to the electrolyte and thus enhance ion and electron diffusion. The open geometry between the arrays allows easier electrolyte penetration into the inner region of the electrode, increasing the utilization of the active materials. Besides, the nanowires grown on the nanoflakes can also afford facile electron transport for Faradic reaction, leading to faster kinetics. Second, the unique hetero-structured $NiCo_2O_4$ is expected to offer richer active sites for electrochemical reactions, including contributions from both the nanoflakes and nanowires. The richer active sites results in a higher specific capacitance result. Third, the structure directly grown on the nickel foam ensures good mechanical adhesion and electrical connection to the current collector and, therefore, avoids the use of polymer binders and conducting additives. Forth, in the $NiCo_2O_4$ hetero-structure array, the nanoflakes connect with each other, forming a flake-network. The nanoflakes support each other, making the structure stable. On the other hand, the nanowires grown at the edge of the nanoflakes with a cross configuration can also make the structure stable. Such a stable and connecting structure helps to alleviate the structure damage caused by volume expansion during cycling process, resulting in an enhanced stability. Because of these intriguing advantages, the porous $NiCo_2O_4$ hetero-structure array with excellent electrochemical performance has been achieved.

Fig. 6. (a) CV curves of porous $NiCo_2O_4$ hetero-structure array in the potential region of 0–0.6 V at a scanning rate of 1 mV s^{-1}, (b) discharge curves of the $NiCo_2O_4$ array at different discharge current densities, (c) specific capacitance and capacity retention as a function of current density, (d) Ragone plot of the porous $NiCo_2O_4$ hetero-structure array.

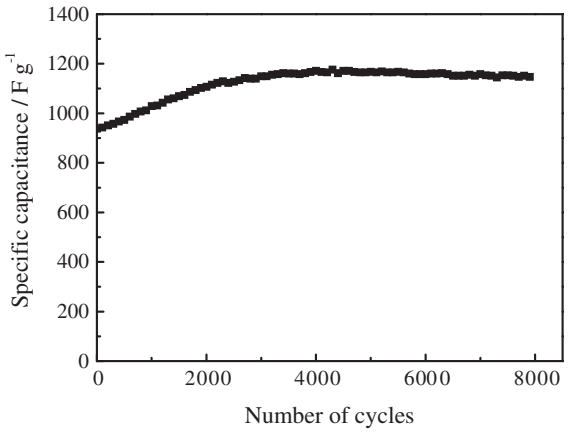

Fig. 7. Cyclability of the porous $NiCo_2O_4$ hetero-structure array between 0 and 0.5 V at a current density of 2 A g^{-1}.

4. Conclusions

In summary, a porous $NiCo_2O_4$ nanoflake–nanowire array has been fabricated via a facile hydrothermal method followed by a suitable annealing treatment. Relative Ni enrichment reveals in the nanoflakes, while the nanowires maintain a much higher Co:Ni atomic ratio which is close to the stoichiometric molar ratio. A mechanism for the unique hetero-structure formation is put forward which involves the K_{sp} and self-assembly. The porous $NiCo_2O_4$ heterostructure array is an attractive material for supercapacitors with high capacitance and excellent cyclability. Its outstanding pseudocapacitive performance comes from the porous hetero-structure configuration, which provides fast ion and electron transfer, large number of active sites and good strain accommodation.

Acknowledgments

The authors would like to acknowledge financial support from the Key Science and Technology Innovation Team of Zhejiang Province (2010R50013).

Appendix A. Supplementary data

Supplementary data related to this article can be found at http://dx.doi.org/10.1016/j.jpowsour.2013.03.106.

References

[1] S. Makino, Y. Yamauchi, W. Sugimoto, J. Power Sources 227 (2013) 153.
[2] T.-Y. Wei, C.-H. Chen, H.-C. Chien, S.-Y. Lu, C.-C. Hu, Adv. Mater. 22 (2012) 347.
[3] G.P. Xiong, K.P.S.S. Hembram, R.G. Reifenberger, T.S. Fisher, J. Power Sources 227 (2013) 254.
[4] D.F. Yang, J. Power Sources 228 (2013) 89.
[5] X.H. Xia, J.P. Tu, Y.Q. Zhang, Y.J. Mai, X.L. Wang, C.D. Gu, X.B. Zhao, RSC Adv. 2 (2012) 1835.
[6] X.H. Xia, J.P. Tu, Y.J. Mai, X.L. Wang, C.D. Gu, X.B. Zhao, J. Mater. Chem. 21 (2011) 9319.
[7] H. Jiang, J. Ma, C.Z. Li, Adv. Mater. 24 (2012) 4197.
[8] X.H. Xia, J.P. Tu, Y.J. Mai, R. Chen, X.L. Wang, C.D. Gu, X.B. Zhao, Chem. Eur. J. 17 (2011) 10898.
[9] R.R. Salunkhe, K. Jang, H. Yu, S. Yu, T. Ganesh, S.H. Han, H. Ahn, J. Alloys Compd. 509 (2011) 6677.
[10] X.H. Xia, J.P. Tu, X.L. Wang, C.D. Gu, X.B. Zhao, J. Mater. Chem. 21 (2011) 671.
[11] Y.Q. Zhang, X.H. Xia, J. Kang, J.P. Tu, Chin. Sci. Bull. 57 (2012) 4215.
[12] Y.Q. Zhang, X.H. Xia, J.P. Tu, Y.J. Mai, S.J. Shi, X.L. Wang, C.D. Gu, J. Power Sources 199 (2012) 413.
[13] V. Gupta, S. Gupta, N. Miura, J. Power Sources 195 (2010) 3757.
[14] X.H. Xia, J.P. Tu, X.L. Wang, C.D. Gu, X.B. Zhao, Chem. Commun. 47 (2011) 5786.
[15] W. Du, R.M. Liu, Y.W. Jiang, Q.Y. Lu, Y.Z. Fan, F. Gao, J. Power Sources 227 (2013) 101.
[16] X.J. Zhang, W.H. Shi, J.X. Zhu, W.Y. Zhao, J. Ma, S. Mhaisalkar, T.L. Maria, Y.H. Yang, H. Zhang, H.H. Hng, Q.Y. Yan, Nano Res. 3 (2010) 643.
[17] C.Z. Yuan, X.G. Zhang, L.H. Su, B. Gao, L.F. Shen, J. Mater. Chem. 19 (2009) 5772.
[18] P.K. Nayak, N. Munichandraiah, J. Solid State Electrochem. 16 (2012) 2739.
[19] Q. Li, Z.L. Wang, G.R. Li, R. Guo, L.X. Ding, Y.X. Tong, Nano Lett. 12 (2012) 3803.
[20] B.G. Choi, Y.S. Huh, W.H. Hong, H.J. Kim, H.S. Park, Nanoscale 4 (2012) 5394.
[21] X. Wang, X.D. Han, M.F. Lim, N.D. Singh, C.L. Gan, M. Jan, P.S. Lee, J. Phys. Chem. C 116 (2012) 12448.
[22] Q. Che, F. Zhang, X.G. Zhang, X.J. Lu, B. Ding, J.J. Zhu, Acta Phys. Chim. Sin. 28 (2012) 837.
[23] J.W. Xiao, S.H. Yang, J. Mater. Chem. 22 (2012) 12253.
[24] J.X. Li, M. Yang, J.P. Wei, Z. Zhou, Nanoscale 4 (2012) 4498.
[25] Z.Y. Lu, W. Zhu, X.D. Lei, G.R. Williams, D. O'Hare, Z. Chang, X.M. Sun, X. Duan, Nanoscale 4 (2012) 3640.
[26] X.H. Xia, J.P. Tu, Y.Q. Zhang, X.L. Wang, C.D. Gu, X.B. Zhao, H.J. Fan, ACS Nano 6 (2012) 5531.
[27] Y. Sharma, N. Sharma, G.V. Subba Rao, B.V.R. Chowdari, Adv. Funct. Mater. 17 (2007) 855.
[28] L. Zhou, D.Y. Zhao, X.W. Lou, Adv. Mater. 24 (2012) 745.
[29] Y.C. Qiu, S.H. Yang, H. Deng, L.M. Jin, W.S. Li, J. Mater. Chem. 20 (2010) 4439.
[30] G.R. Li, Z.L. Wang, F.L. Zheng, Y.N. Ou, Y.X. Tong, J. Mater. Chem. 21 (2011) 4217.
[31] N. Du, Y.F. Xu, H. Zhang, J.X. Yu, C.X. Zhai, D.R. Yang, Inorg. Chem. 50 (2011) 3320.
[32] C.H. Wang, X. Zhang, D.C. Zhang, C. Yao, Y.W. Ma, Electrochim. Acta 63 (2012) 220.
[33] Y.Q. Wu, X.Y. Chen, P.T. Ji, Q.Q. Zhou, Electrochim. Acta 56 (2011) 7517.
[34] S.K. Chang, K.T. Lee, Z. Zainal, K.B. Tan, N.A. Yusof, W.M.D.W. Yusoff, J.F. Lee, N.L. Wu, Electrochim. Acta 67 (2012) 67.
[35] J.W. Xiao, S.H. Yang, RSC Adv. 1 (2011) 588.
[36] H.L. Wang, Q.M. Gao, L. Jiang, Small 7 (2011) 2454.
[37] J. Chang, J. Sun, C.H. Xu, H. Xu, L. Gao, Nanoscale 4 (2012) 6786.
[38] Q.F. Wang, B. Liu, X.F. Wang, S.H. Ran, L.M. Wang, D. Chen, G.Z. Shen, J. Mater. Chem. 22 (2012) 21647.
[39] G.Q. Zhang, H.B. Wu, H.E. Hoster, M.B. Chan-Park, X.W. Lou, Energy Environ. Sci. 5 (2012) 9453.
[40] C.Z. Yuan, J.Y. Li, L.R. Hou, L. Yang, L.F. Shen, X.G. Zhang, J. Mater. Chem. 22 (2012) 16084.
[41] Y. Ren, Z. Ma, P.G. Bruce, Chem. Soc. Rev. 41 (2012) 4909.
[42] R.R. Salunkhe, K. Jang, S.W. Lee, H. Ahn, RSC Adv. 2 (2012) 3190.
[43] H.W. Wang, Z.A. Hu, Y.Q. Chang, Y.L. Chen, H.Y. Wu, Z.Y. Zhang, Y.Y. Yang, J. Mater. Chem. 21 (2011) 10504.
[44] T. Wu, J.Y. Li, L.R. Hou, C.Z. Yuan, L. Yang, X.G. Zhang, Electrochim. Acta 81 (2012) 172.
[45] H. Jiang, J. Ma, C.Z. Li, Chem. Commun. 48 (2012) 4465.
[46] B. Cui, H. Lin, J.B. Li, X. Li, J. Yang, J. Tao, Adv. Funct. Mater. 18 (2008) 1440.